Journal of Solid State Chemistry 182 (2009) 2176–2184

Contents lists available at ScienceDirect

Journal of Solid State Chemistry

journal homepage: www.elsevier.com/locate/jssc

A TEM investigation of the $(Bi_{1-x}Sr_x)Fe^{3+}O_{3-x/2}$, $0.2 \leq x \leq 0.67$, solid solution and a suggested superspace structural description thereof

R.L. Withers [a,*], L. Bourgeois [b], K. Balamurugan [c], N. Harish Kumar [c], P.N. Santhosh [c], P.M. Woodward [d]

[a] Research School of Chemistry, Australian National University, Canberra, ACT 0200, Australia
[b] Monash Centre for Electron Microscopy and Department of Materials Engineering, Monash University, Victoria 3800, Australia
[c] Department of Physics, Indian Institute of Technology Madras, Chennai, Tamil Nadu 600036, India
[d] Department of Chemistry, Ohio State University, 100 West 18th Ave., Columbus, OH 43210-1185, USA

ARTICLE INFO

Article history:
Received 16 February 2009
Received in revised form
11 May 2009
Accepted 17 May 2009
Available online 22 May 2009

Keywords:
Modulated structure
Intergrowth compound
Continuous solid solution
TEM investigation
Ferrites

ABSTRACT

A careful transmission electron microscopy (TEM) investigation of an incommensurately modulated member of the $(Bi_{1-x}Sr_x)Fe^{3+}O_{3-x/2}\square_{x/2}$, $0.2 \leq x \leq 0.67$, solid solution has been carried out. High resolution (HR) TEM imaging is used to show the presence of at least 6-fold twinning on a rather fine (~5 nm) scale. The (3+1)-d superspace group symmetry is suggested to be $Pmmm(0,\frac{1}{2},\gamma)$ or one of the non-centrosymmetric sub-groups thereof, namely $P2mm(0,\frac{1}{2},\gamma)$, $Pm2m(0,\frac{1}{2},\gamma)$, $Pmm2(0,\frac{1}{2},\gamma)$ and $P222(0,\frac{1}{2},\gamma)$. A superspace construction is then used to propose the nature of the local compositional ordering and, hence, of the oxygen-deficient slab that intergrows with the perovskite slab to produce the observed solid solution phase. The proposed compositional superspace atomic surfaces can be used to produce model structures at any composition within the solid solution range.

1. Introduction

The characteristic ability of the perovskite structure type (ideal composition ABX_3) to regularly intergrow with layers, or slabs, of alternate local structure type along particular parent perovskite directions often leads to a range of compositionally closely related compounds, or even compositionally continuous, solid solution phases [1–5]. Particularly well-known examples include Aurivillius [1,2] and Ruddlesden–Popper [3] type phases wherein perovskite blocks regularly intergrow along an ideal $\langle 001 \rangle_p$ direction (in what follows, the subscript p stands for the underlying parent perovskite structure type) with Bi_2O_2 and NaCl type layers, respectively. In these cases, the structural basis of the underlying compositional flexibility is now well understood, particularly since the application of the superspace approach to such problems [4,5]. One example, where the structural basis of compositional flexibility is not yet understood, is provided by the recent report of a complex $(Bi_{1-x}Sr_x)Fe^{3+}O_{3-x/2}$, $0.2 \leq x \leq 0.67$, perovskite related, solid solution phase [6]. There has been much recent interest in bismuth containing ferrite phases such as this, as a result of the multiferroic properties of $BiFeO_3$ itself, as well as in $BiFeO_3$-based multiferroics [7–9].

The ability of Fe to adopt a range of distinct local co-ordination environments e.g. tetrahedral (IV), pyramidal (V) or octahedral (VI) [10], within the same underlying, average perovskite type, framework sub-structure is of particular relevance in this context. The structures of $Sr_2Fe_2O_5$ [11], with a $\sqrt{2}a_p \times \sqrt{2}a_p \times 4a_p$ supercell, and $LaCa_2Fe_3O_8$ [12] with a $\sqrt{2}a_p \times \sqrt{2}a_p \times 3a_p$ supercell, are shown in projection along the shorter of the $\sqrt{2}a_p$ directions in Figs. 1a and b, respectively. In both cases, individual layers of tetrahedrally co-ordinated Fe atoms (formally obtainable from a hypothetical octahedral layer by the systematic removal of alternate $[110]_p$ rows of oxygen ions, labelled with the symbol □ in Figs. 1a and b, respectively) intergrow with a perovskite slab. In the case of $Sr_2Fe_2O_5$ (Fig. 1a), the perovskite slab is one octahedron in height, whereas in the case of $LaCa_2Fe_3O_8$ (Fig. 1b) it is two octahedra in height. Note that such an oxygen vacancy ordering mechanism always leads to a $\sqrt{2}a_p \times \sqrt{2}a_p$ basal plane supercell and that the *c*-axis repeat distance, and hence the size of the supercell, is also directly related to the distribution of oxygen vacancies (labelled with the symbol □) in both cases.

A very recent, careful investigation [10] of one composition within the above reported solid solution field, $(Bi_{1/3}Sr_{2/3})Fe^{3+}O_{2.667}\square_{0.333}$, as well as a different composition with a closely related structure, $(Bi_{1/2}Ca_{1/2})Fe^{3+}O_{2.75}\square_{0.25}$, suggests the distinct possibility that both the $(Bi_{1-x}Sr_x)Fe^{3+}O_{3-x/2}\square_{x/2}$ and $(Bi_{1-x}Ca_x)Fe^{3+}O_{3-x/2}\square_{x/2}$ systems possess considerable compositional flexibility. As mentioned above, this hypothesis is supported by the earlier report of a continuous, perovskite type, $(Bi_{1-x}Sr_x)$

* Corresponding author.
E-mail address: withers@rsc.anu.edu.au (R.L. Withers).

0022-4596/$ - see front matter © 2009 Elsevier Inc. All rights reserved.
doi:10.1016/j.jssc.2009.05.019

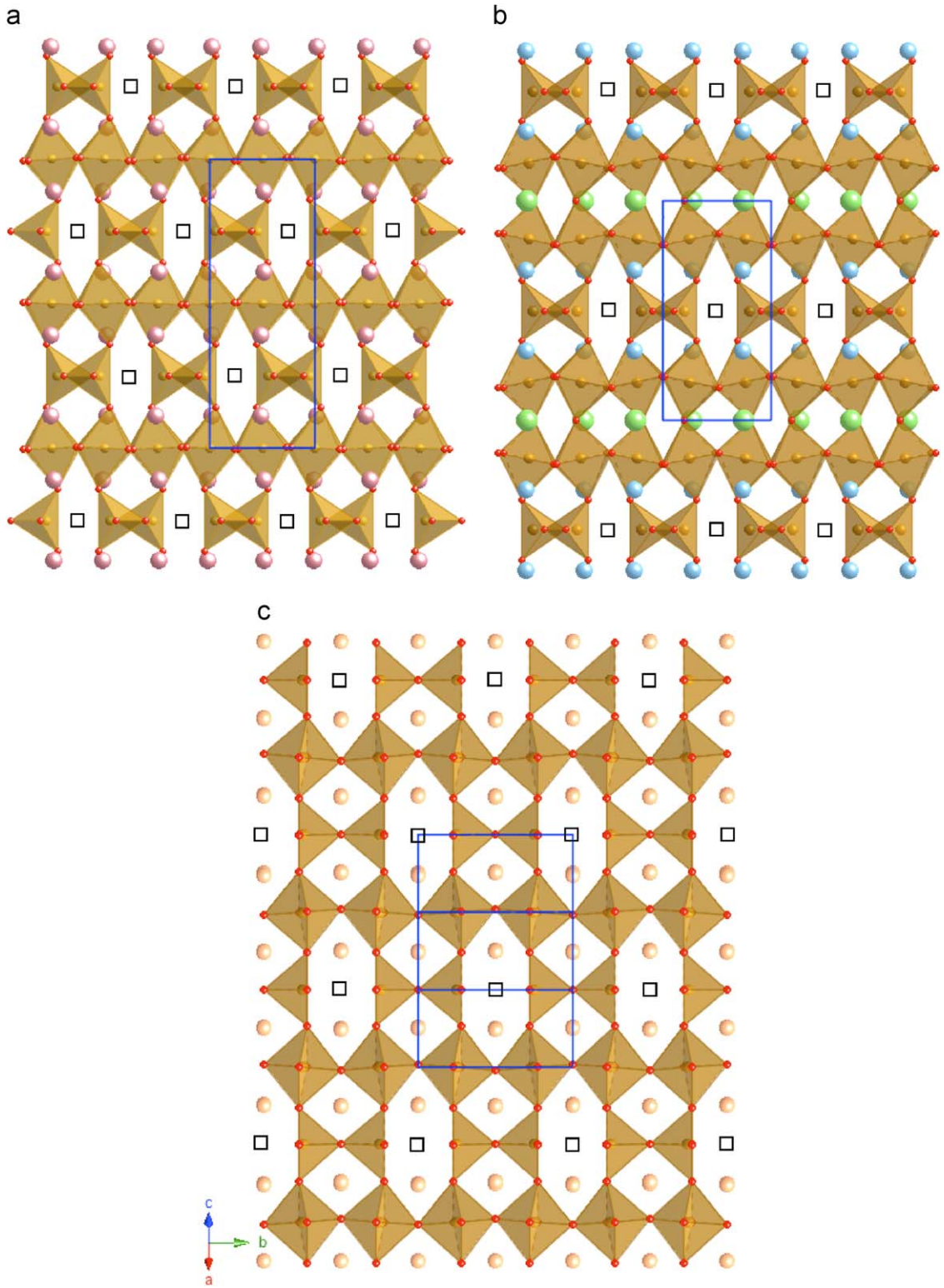

Fig. 1. (a) and (b) show the $\sqrt{2}a_p \times \sqrt{2}a_p \times 4a_p$ and $\sqrt{2}a_p \times \sqrt{2}a_p \times 3a_p$ structures of $Sr_2Fe_2O_5$ and $LaCa_2Fe_3O_8$ in projection along the shorter of the $\sqrt{2}a_p$ directions. Note the regular intergrowth of a perovskite block with an oxygen deficient tetrahedral layer. The FeO_6 octahedra and FeO_4 tetrahedra are shown in brown in both (a) and (b). The Sr ions are represented by the large pink balls and the O ions by the small red balls in (a) while the La ions are represented by the large green balls, the Ca ions by the medium sized blue balls and the O ions by the small red balls in (b). (c) shows a typical $\{001\}_p$ type layer of $Sr_4Fe_4O_{11}$ involving the intergrowth of an octahedral perovskite block with an oxygen deficient pyramidal block. The FeO_6 octahedra and FeO_5 square pyramids are shown in brown in (c), while the Sr ions are represented by the large pink balls and the O ions by the small red balls. The oxygen vacancies (with respect to an ideal perovskite structure) are labelled with the symbol □ in (a)–(c). (For interpretation of the references to colour in this figure legend, the reader is referred to the web version of this article.)

$Fe^{3+}O_{3-x/2}\square_{x/2}$ solid solution phase over the entire composition range $0.2 \leq x \leq 0.67$ [6]. Interestingly, both of the above compounds adopt unit cells with a $2a_p \times 2a_p$ basal plane supercell, rather than the expected $\sqrt{2}a_p \times \sqrt{2}a_p$ supercell [10]. This suggests an oxygen vacancy ordering mechanism, and hence intergrowth structural type, that is quite distinct from those

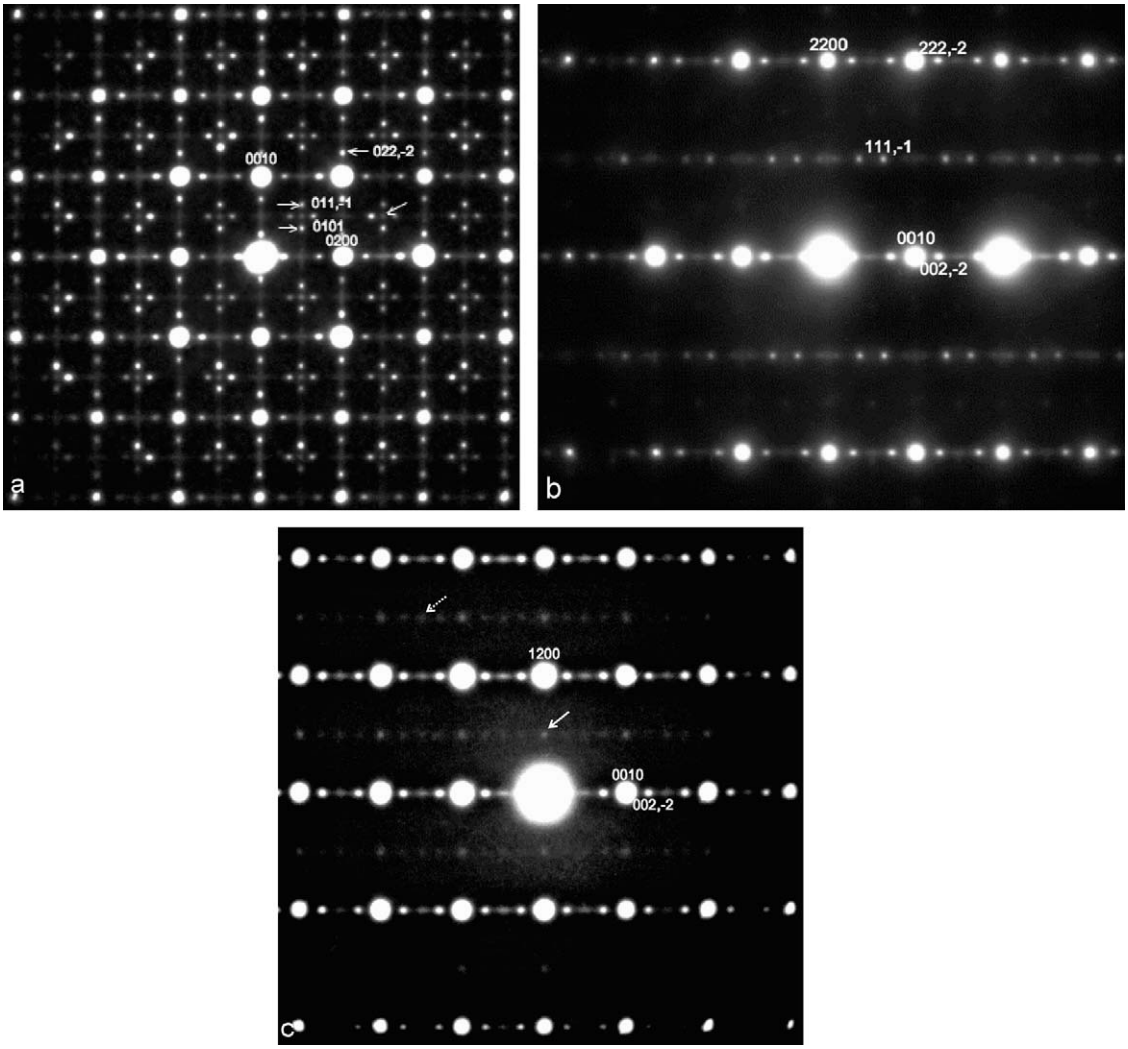

Fig. 2. (a) $\langle 100\rangle_p$, (b) $\langle -1,2,0\rangle_p$ and (c) $\langle -1,1,0\rangle_p$ zone axis EDP's typical of the $(Bi_{1-x}Sr_x)Fe^{3+}_1O_{3-x/2}\square_{x/2}$, $x\sim0.55$, sample. The EDP's are indexed with respect to the (3+1)-d reciprocal lattice basis vector set $M^* = \{\mathbf{a}^*_\mathbf{p}, \frac{1}{2}\mathbf{b}^*_\mathbf{p}, \mathbf{c}^*_\mathbf{p}, \mathbf{q}\sim0.356\mathbf{c}^*_\mathbf{p}\}$.

observed in $Sr_2Fe_2O_5$ and $LaCa_2Fe_3O_8$. Lepoittevin et al. (see Fig. 7a of [10]), on the bais of XRD and HRTEM results, suggest the intergrowth of a perovskite block with a unique one layer high, pyramidally co-ordinated Fe layer, as is also characteristic of $\{001\}_p$ type layers of $Sr_4Fe_4O_{11}$ [11] (see e.g. Fig. 1c).

In this paper, we first report the results of a careful TEM investigation of an incommensurate member of the proposed $(Bi_{1-x}Sr_x)Fe^{3+}O_{3-x/2}\square_{x/2}$, $0.2\leq x\leq 0.67$, solid solution phase focussing on the determination of its (3+1)-d superspace group symmetry. The TEM results of the previously reported investigation [10] at the $(Bi_{1/3}Sr_{2/3})Fe^{3+}O_{2.667}\square_{0.333}$ ($x=\frac{2}{3}$) and $(Bi_{1/2}Ca_{1/2})Fe^{3+}O_{2.75}\square_{0.25}$ ($x=\frac{1}{2}$) compositions are used to guide this determination. A superspace approach is then used to propose a plausible model for the oxygen vacancy, and associated Bi/Sr, ordering as well as the nature of the oxygen-deficient slab that intergrows with the perovskite slab to produce the observed solid solution phase.

2. Experimental

2.1. Sample fabrication

The nominally $Bi_{0.5}Sr_{0.5}FeO_3$ sample was synthesized by solid state reaction. Bi_2O_3 (99.999%), $SrCO_3$ (99.9+%) and Fe_3O_4 (99.99%) (Sigma-Aldrich) reagents were used in the synthesis. A 5 wt% of excess Bi_2O_3 was added to the stoichiometric proportion of the reagents in order to compensate for presumed Bi evaporation during heat treatment of the mixed reagents [13]. This mixture was initially heat treated at 873 K for 12 h. A final heat treatment was then performed at 1223 K for 48 h with intermediate grinding to ensure homogeneity.

2.2. Electron probe micro-analysis

In order to check for homogeneity as well as to establish the exact resultant composition, the sample was also quantitatively analysed via electron probe micro analysis (EPMA). A JEOL 6400 scanning electron microscope (SEM) equipped with an Oxford Instruments light element EDS detector and Link ISIS SEMquant software was used. The sample was embedded in resin and polished to a $<1\,\mu m$ finish with corundum. More than 10 separate spot analyses were carried out at 15 kV and 1 nA using Bi_2O_3, celestite ($SrSO_4$) and Fe_2O_3 as calibration standards.

2.3. X-ray powder diffraction

X-ray powder diffraction data of the sample was collected, over the 2θ range 10–90° with a step size of 0.0167°, using a

PANalytical (X'Pert Pro) Powder X-ray diffractometer and Cu$K\alpha$ radiation.

2.4. Transmission electron microscopy

Electron diffraction was carried out in a Philips EM 430 transmission electron microscope (TEM) operating at 300 kV on crushed portions of the sample dispersed onto holey carbon coated copper grids. High resolution (HR) TEM images were collected on a JEOL 2100F TEM operating at 200 kV. HRTEM simulations were performed via the multi-slice method [14] using the JEMS software package [15].

3. Results

SEM analysis showed the sample to be quite homogeneous both from the imaging and analysis points of view with an average composition $Bi_{0.54(1)}Sr_{0.46(1)}Fe_{1.00(1)}O_{2.77}$ (the average of 10 separate spot analyses with the error bars giving a measure of the observed narrow compositional spread). The oxygen content in the above formula was derived from the analysed metal ion ratios assuming the Fe valence state to be +3, following the ceremetric titration and Mossbauer results given in [6,10]. XRD gave a metrically cubic average perovskite structure with cubic unit cell dimension $a_p = 3.945$ Å. Superlattice lines were not detectable in the powder XRD data.

Fig. 2 shows (a) $\langle 100\rangle_p$, (b) $\langle -1,2,0\rangle_p$ and (c) $\langle -1,1,0\rangle_p$ zone axis electron diffraction patterns (EDP's) typical of the $(Bi_{1-x}Sr_x)Fe^{3+}O_{3-x/2}\square_{x/2}$, $x\sim0.46$, sample. (Note that indices are given here, and in what follows, with commas separating individual indices when at least one of the indices is negative to avoid possible misinterpretation. Otherwise, no commas are used). At first glance, such EDP's are reminiscent of a (3+3)-d incommensurately modulated structure (see e.g. [16]) with satellite reflections running along all three $\langle 001\rangle_p^*$ directions of reciprocal space simultaneously and characterized by incommensurate primitive primary modulation wave-vectors of $\langle 0,\frac{1}{2},0.356(1)\rangle_p^*$ type. Note the strong similarity of Fig. 2a to the equivalent $\langle 100\rangle_p$ zone axis EDP of $(Bi_{1/3}Sr_{2/3})Fe_1^{3+}O_{2.667}\square_{0.333}$ shown in Fig. 2a of [10]. There are, however, two significant differences. Firstly, the $\mathbf{G}\pm\frac{1}{2}\langle 110\rangle_p^*$ and $\mathbf{G}\pm\frac{1}{2}\langle 100\rangle_p^*$ 'satellite reflections' (one such reflection is arrowed, but not labelled, in Fig. 2a) are very much weaker in our case than in Fig. 2a of [10] (indeed these 'satellite reflections' are barely visible at all in our case, see Fig. 2a). Secondly, the incommensurate $\langle 0,\frac{1}{2},0.356(1)\rangle_p^*$ primitive primary modulation wave-vectors in our case appear to be commensurate in the latter $(Bi_{1/3}Sr_{2/3})Fe_1^{3+}O_{2.667}\square_{0.333}$ case and given by $\langle 0,\frac{1}{2},\frac{1}{3}=0.333\rangle_p^*$ (see Fig. 2a of [10]).

HRTEM imaging down a $\langle 100\rangle_p$ direction, in agreement with the results of [10], shows that the material is at least triply twinned on quite a fine, ~5–10 nm, scale (see e.g. Fig. 3a; the corresponding fast Fourier transform (FFT) of the whole image is shown in Fig. 3b and a selected area EDP from a much larger region including the image area is shown in Fig. 3c). Note that the FFT exhibits the same low-angle reflections as the EDP, implying that the spatial frequencies able to be imaged by the microscope are representative of those deduced from the EDP. In particular, incommensurate superlattice 'fringes' of periodicity $a_p/(1-2\times0.356)\sim3.47$ $a_p\sim13.7$ Å, typically running largely along only one or other of the two $\langle 001\rangle_p^*$ directions of reciprocal space excited in any one such $\langle 100\rangle_p$ type image, are apparent in different regions of the image (see Fig. 3a). In other areas, no obvious superlattice fringes are evident at all (see e.g. the highlighted region at the top of Fig. 3a) suggesting that the incommensurate component of the modulation in such regions is running primarily along the third $\langle 001\rangle_p^*$ direction of reciprocal space i.e. along the projection direction.

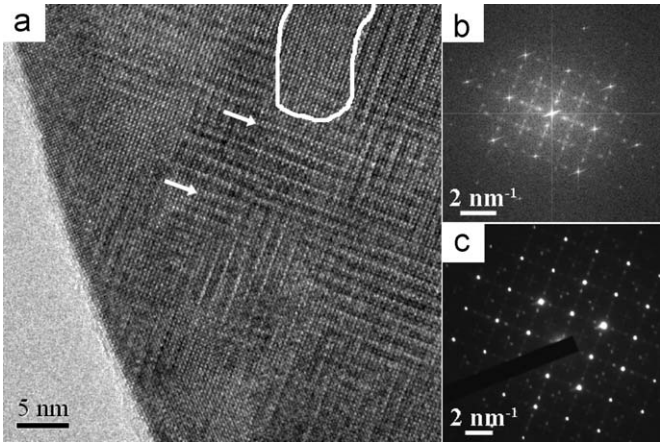

Fig. 3. (a) A typical HREM image down a $\langle 100\rangle_p$ direction. Note that the material is at least triply twinned on quite a fine, ~5–10 nm, scale. (b) The corresponding fast Fourier transform (FFT) of the whole image. A selected area EDP from a much larger region including the image area is shown in (c).

Fig. 4 shows an attempt to identify individual single domain regions by generating inverse FFT's (iFFT's) from different parts of the full FFT (see the bottom left hand inserts in Figs. 4a–c). From such images, it is clearly no easy task to find a truly non-overlapped single domain region. It is nonetheless clear that the incommensurate component of the primitive primary modulation wave-vector runs along only one of the three possible $\langle 001\rangle_p^*$ directions in any one local region (see e.g. the framed regions in Fig. 4, where each colour corresponds to a different incommensurate $\langle 001\rangle_p^*$ direction) and thus $(Bi_{1-x}Sr_x)Fe_1^{3+}O_{3-x/2}\square_{x/2}$, $x\sim0.46$, can only be described as a (3+1)-d incommensurately modulated structure [17], rather than a (3+3)-d incommensurately modulated structure [16].

At this stage, however, there remain two possible primitive primary modulation wave-vectors associated with a particular $0.356\mathbf{c}_p^*$ incommensurate wave-vector component, namely $\mathbf{q}_{prim}^1 = [\frac{1}{2},0,0.356]_p^*$ and $\mathbf{q}_{prim}^2 = [0,\frac{1}{2},0.356]_p^*$. The question becomes, do both these potential primitive primary modulation wave-vectors locally co-exist or does only one exist on the local scale leading to a rather more subtle, presumably finer scale still, form of twinning? Note that along the superlattice fringes themselves there are often regions that exhibit a clear doubling of the parent perovskite repeat distance, associated with the rational $[0,\frac{1}{2}]_p^*$ component of the primitive primary modulation wave-vector $[0,\frac{1}{2},0.356]_p^*$ and corresponding to a $[100]_p$ zone axis orientation (see e.g. the top arrowed region in Fig. 3a). Equally, however, there are also regions where no such doubling is apparent, corresponding to an $[010]_p$ zone axis orientation (see e.g. the bottom arrowed region to the left in Fig. 3a). Such observations strongly suggest that only one of the two possible primitive primary modulation wave-vectors given above locally exists. Similar behaviour also occurs in the cases of $(Bi_{1/3}Sr_{2/3})Fe_1^{3+}O_{2.667}\square_{0.333}$ (cf. Fig. 3a with Fig. 3c in [10]) and $(Bi_{1/2}Ca_{1/2})Fe_1^{3+}O_{2.75}\square_{0.25}$ (cf. Fig. 6b with Fig. 6c in [10]) and shows that the correct local symmetry in both these systems is orthorhombic rather than tetragonal. We have chosen this unique primitive primary modulation wave-vector to be $\mathbf{q}_{prim} = [0,\frac{1}{2},0.356]_p^*$ in our case.

The EDP's in Fig. 2 are thus indexed with respect to the (3+1)-d reciprocal lattice basis vector set $M^* = \{\mathbf{a}_p^*, \frac{1}{2}\mathbf{b}_p^*, \mathbf{c}_p^*, \mathbf{q}\sim0.356\mathbf{c}_p^*\}$. Note that all the EDP's in Fig. 2 are necessarily obtained from areas much larger than the true single domain regions and are thus inevitably at least 6-fold twinned making it rather difficult to be

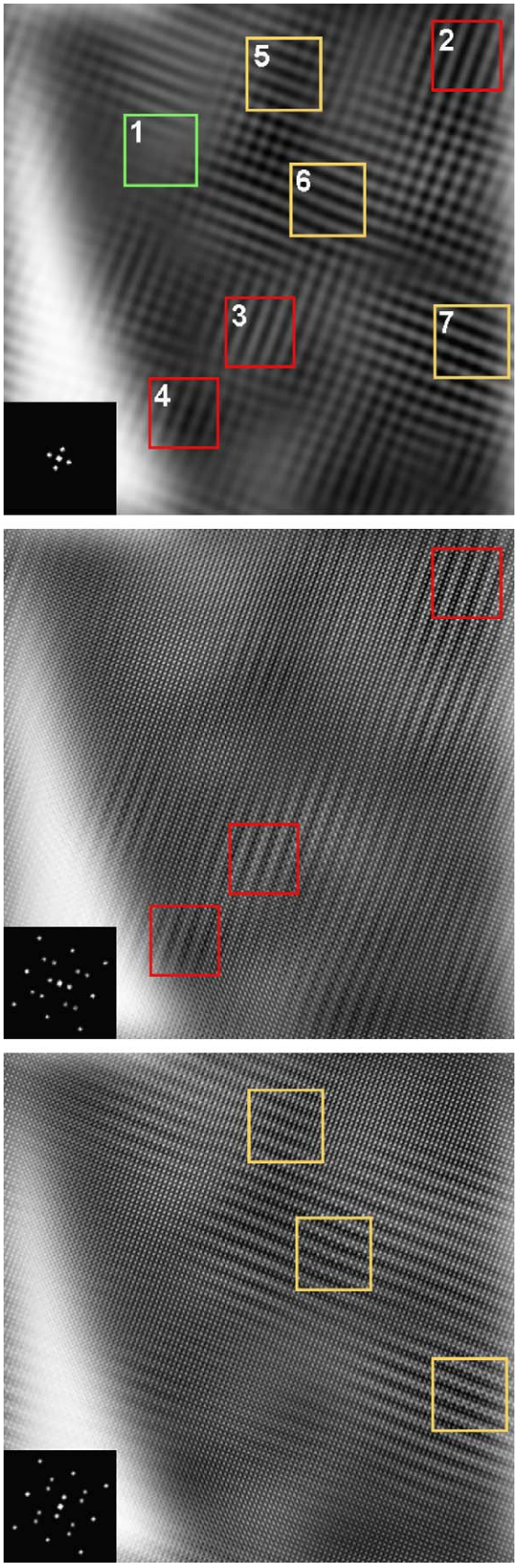

Fig. 4. Inverse FFT's of the HREM image in Fig. 3a generated from different parts of the full FFT (see the bottom left hand inserts in (a)–(c)).

sure which reflections belong to which symmetry equivalent (in terms of the underlying parent perovskite structure) zone axis orientation, particularly when the strong possibility/probability of twinning along the projection axis direction is taken into account (see e.g. Fig. 4a). Note that the local observation of a doubling along the [010] but not along the [100] direction suggests that only second order harmonic satellite reflections can occur when looking down the [010] direction i.e. the columns of satellite reflections running along the $\mathbf{c}_p^*$ direction in Fig. 2a will only exist in the same columns as the parent Bragg reflections in [010] zone axis EDP's.

The only systematic extinction condition observed under the above assumptions is $F(HKLM) = 0$ unless $K+M$ even implying the superspace centreing operation $\{x_1, x_2 + \frac{1}{2}, x_3, x_4 + \frac{1}{2}\}$ and giving rise to possible superspace group symmetries $Pmmm(0, \frac{1}{2}, \gamma)$ or the non-centrosymmetric sub-groups thereof, namely $P2mm(0, \frac{1}{2}, \gamma)$, $Pm2m(0, \frac{1}{2}, \gamma)$, $Pmm2(0, \frac{1}{2}, \gamma)$ and $P222(0, \frac{1}{2}, \gamma)$ [17]. The generating elements of the superspace group $Pmmm(0, \frac{1}{2}, \gamma)$ [17] can be chosen to be $\{x_1, x_2 + \frac{1}{2}, x_3, x_4 + \frac{1}{2}\}$, $\{-x_1, x_2, x_3, x_4\}$, $\{x_1, \frac{1}{2} - x_2, x_3, x_4\}$, $\{x_1, x_2, -x_3, -x_4 + \frac{1}{2} + 2\phi\}$ and $\{-x_1, -x_2, -x_3, -x_4 + 2\phi\}$, respectively, where ϕ is the so-called global phase [4,5].

As mentioned above, there is some evidence for very weak additional $\frac{1}{2}[110]_p^*$ and $\frac{1}{2}[111]_p^*$ modulations, presumably associated with octahedral and pyramidal rotations, in the form of extremely weak, barely detectable $\mathbf{G} \pm \frac{1}{2}[110]_p^*$ and $\mathbf{G} \pm \frac{1}{2}[111]_p^*$ satellite reflections (arrowed, but not labelled, in Figs. 2a and c). For the purposes of what follows, however, these modulations will not be taken into account as they are clearly independent of the much stronger incommensurate modulation or with the oxygen vacancy and Bi^{3+}/Sr^{2+} ordering responsible.

4. A superspace interpretation

Having established a probable superspace group symmetry, i.e. $Pmmm(0, \frac{1}{2}, \gamma)$, a superspace approach is now used to investigate the compositional nature of the oxygen-deficient slab that intergrows with the perovskite slab to produce the observed $(Bi_{1-x}Sr_x)Fe_1^{3+}O_{3-x/2}\square_{x/2}$, $0.2 \leq x \leq 0.67$, solid solution phase as well as the possible layer stacking sequences thereof. The primitive primary modulation wave-vector $\mathbf{q}_{prim} = [0, \frac{1}{2}, 0.356]_p^*$ in our case, $[0, \frac{1}{2}, 0.333]_p^*$ in the case of $(Bi_{1/3}Sr_{2/3})Fe_1^{3+}O_{2.667}\square_{0.333}$ and $[0, \frac{1}{2}, 0.375]_p^*$ in the closely related case of $(Bi_{1/2}Ca_{1/2})Fe_1^{3+}O_{2.75}\square_{0.25}$ (see Figs. 3 and 4 of [10], respectively). This composition dependence of the primitive primary modulation wave-vector strongly suggests that the intergrown layers as well as the layer stacking sequences characteristic of the $(Bi_{1-x}Sr_x)Fe_1^{3+}O_{3-x/2}\square_{x/2}$ solid solution are determined by composition and follow a well defined crystal chemical rule (see e.g. [4,5]). The results of [10], i.e. $\gamma = \frac{3}{8}$ for $x = \frac{1}{2}$ and $\gamma = \frac{1}{3}$ for $x = \frac{2}{3}$, suggest a simple linear relationship between the primary modulation wave-vector magnitude, γ, and the overall composition, x, given by $\gamma = \frac{1}{2} - \frac{x}{4}$. The result obtained in the current paper, $\gamma = 0.356(1)$ for $x = 0.46(1)$, however, is not entirely consistent with this relationship and suggests some flexibility in the relationship e.g. $\gamma = \frac{1}{2} - \frac{x}{4}$ implies that x should be 0.576 instead of 0.46(1) for the observed value for γ of 0.356.

The overall $(Bi_{1-x}Sr_x)Fe_1^{3+}O_{3-x/2}\square_{x/2}$ composition of the solid solution field requires that there must be two Sr^{2+} ions per oxygen vacancy. Bond valence sum, or apparent valence (AV), calculations (see e.g. [18,19]), assuming an ideal perovskite structure type with cubic unit cell dimension $a_p = 3.945$ Å and no oxygen vacancies (see Table 1), shows that the Bi^{3+} ions are significantly underbonded (i.e. AV(Bi) = 1.811 instead of 3) whereas the Sr^{2+} ions are essentially ideally bonded (AV(Sr) = 1.953 instead of 2). There are two possibilities for how this might be interpreted. Electrostatic

Table 1
Calculated bond valence sums, or apparent valences (AV's), assuming an ideal perovskite structure type with cubic cell dimension $a_p = 3.945$ Å.

A	AV(*A*)	AV(Fe)	AV(O)
Bi	1.811	3.368	1.726
Sr	1.953	3.368	1.774

R_0 parameters obtained from O'Keeffe and Brese (see [19]).

arguments favour placing the oxygen vacancies near the less positively charged Sr^{2+} sites. Taken at face value the low bond valence sum for Bi^{3+} would also make the creation of an oxygen vacancy in the coordination sphere of a Bi^{3+} ion highly unfavourable. Likewise, given that *ab initio* DFT calculations on related Aurivillius phase type systems (see e.g. [20,21]) have recently shown that energy scales with the square of the so-called global instability index, G_{ii}, defined as the root mean square deviation of the bond valence sums of all ions with respect to their nominal values, it would appear that the oxygen vacancies must necessarily be associated with the Sr^{2+} ions, as also suggested by the overall stoichiometry. On the other hand, the low AV value of Bi^{3+}, even in the absence of oxygen vacancies, strongly suggests the presence of local off-centre displacements of the Bi^{3+} ions consistent with the presence of a stereoactive lone pair. This stereoactive lone pair is believed to result from the strong polarizability of the Bi^{3+} ion in the solid state. It is conceivable that this presumed lone pair could point into the space created by the oxygen vacancy. In that case the oxygen vacancies could form near Bi^{3+} rather than Sr^{2+}. Although what follows is based on the former model, it is not possible to unequivocally rule out the latter.

The *Pmmm*, $a_p \times 2b_p \times c_p$ average structure unit cell (shown in projection along [100] in Fig. 5a, see also Table 2) suggests that oxygen vacancies cannot occur in the $O1_1$ or $O1_2$ sites as this would require a highly unlikely square planar oxygen co-ordination environment for the Fe^{3+} cations. Likewise, vacancies in the apical $O3_1$ and $O3_2$ sites could not explain local orthorhombic rather than tetragonal symmetry or be compatible with the required overall composition. This implies that the oxygen vacancies must be localized to the $O2_1$ and $O2_2$ sites (see Figs. 5b and c and Table 2). The average occupancies of these sites is then $O_{1-x/2}\square_{x/2}$ while that of the $(Bi,Sr)_1$ and $(Bi,Sr)_2$ sites is given by $Bi_{1-x}Sr_x$ (see Table 2).

Taking the above considerations into account, Figs. 6a and b show the implied x_3–x_4 sections of the compositional superspace atomic surfaces (AS's; see e.g. [4,5]) at $x_2 = \frac{1}{4}$ (for $(Bi,Sr)_1$ and $O2_1$, with the Sr occupancy domain shown in yellow and the $O2_1$, oxygen vacancy domain shown in light blue; see Fig. 6a) and at $x_2 = \frac{3}{4}$ (for $(Bi,Sr)_2$ and $O2_2$, with the Sr occupancy domain again shown in yellow and the $O2_1$, oxygen vacancy domain again shown in light blue; see Fig. 6b) drawn for $x = 0.46$ and $\gamma = \frac{5}{14} = 0.3571$. In general, the height of the $O2_1$ oxygen vacancy domain in superspace is given by $\frac{x}{2}$ and runs from $\frac{1}{4} - \frac{x}{2}$ to $\frac{1}{4} + \frac{x}{2}$ in x_4 (see Fig. 6a). Likewise, the height of each of the two $(Bi,Sr)_1$ occupancy domains for Sr are also of height $\frac{x}{2}$ making an overall Sr domain width of x as required by the overall $(Bi_{1-x}Sr_x)Fe^{3+}_1O_{3-x/2}\square_{x/2}$ stoichiometry. Note that the Sr occupancy domains are arranged relative to the $O2_1$ oxygen vacancy domain in such a way that any oxygen vacancy in real space is surrounded above and below by Sr^{2+} ions as is also apparent in the commensurate approximant, *Ammm* structures shown in Figs. 5b and c. Note also that the $O2_2$ and $(Bi,Sr)_2$ occupancy domains or atomic surfaces shown in Fig. 6b are symmetry related to the $O2_1$ and $(Bi,Sr)_1$ occupancy domains shown in Fig. 6a by the superspace centreing operation $\{x_1, x_2 + \frac{1}{2}, x_3, x_2 + \frac{1}{2}\}$.

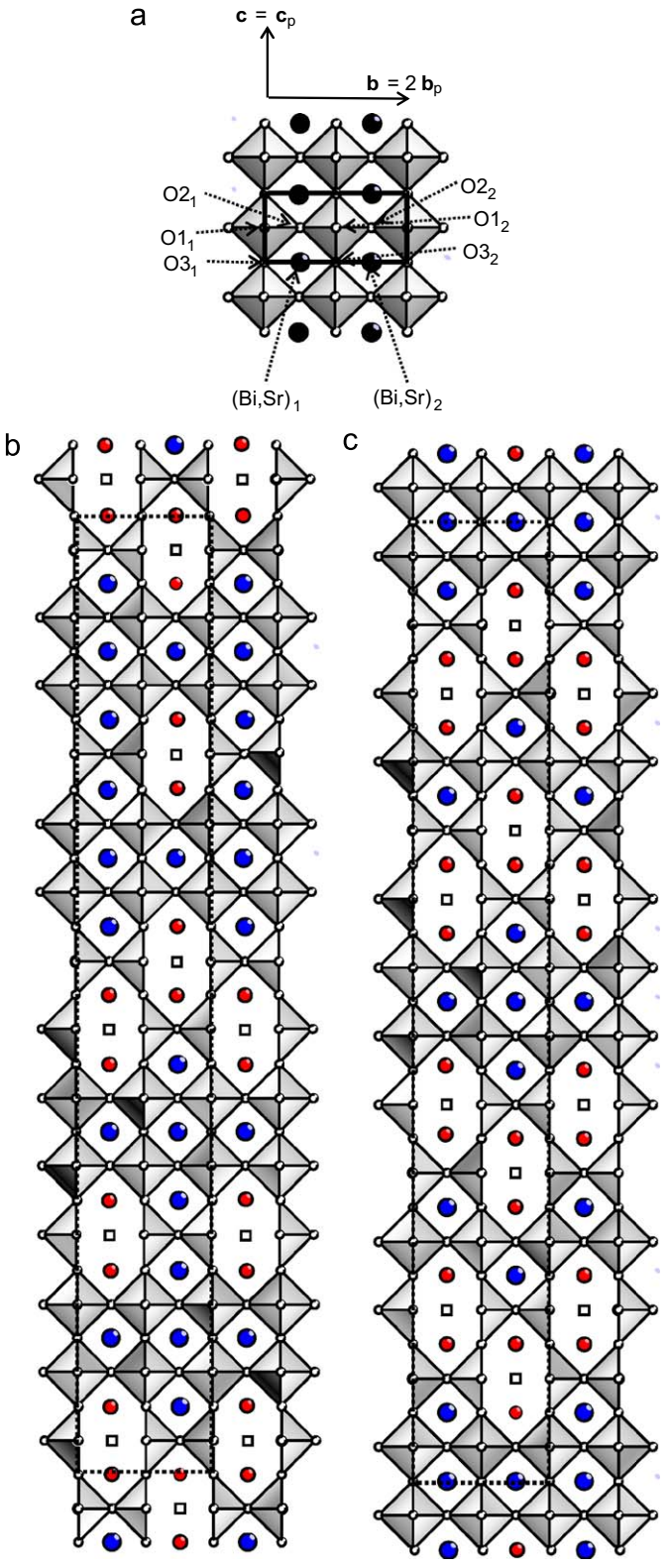

Fig. 5. (a) The *Pmmm*, $a_p \times 2b_p \times c_p$ average structure unit cell (shown in projection along [100]. (b) A [100] projection of the commensurate approximant *Ammm*, $1 \times 2 \times 14$ (see the dashed lines), superstructure predicted by the superspace atomic surfaces shown in Fig. 6 for $x = 0.46$, $\gamma = \frac{5}{14}$ and global phase $\phi = 0$. (c) The *Ammm*, $1 \times 2 \times 14$ (see the dashed lines), superstructure for the global phase $\phi = \frac{1}{4}$ predicted for $x = 0.46$, $\gamma = \frac{5}{14}$. The Bi^{3+} ions are represented by the larger blue balls, the Sr^{2+} ions by the smaller red balls, the oxygen vacancies by the symbol □ while the polyhedra represent the FeO_5 square pyramids and FeO_6 octahedra in (b) and (c), respectively. (For interpretation of the references to colour in this figure legend, the reader is referred to the web version of this article.)

The *Ammm*, $1\times2\times14$, (commensurate approximant) superstructure predicted by this superspace construction for $x=0.46$, $\gamma=\frac{5}{14}$ (the closest, reasonably low order, rational fraction to the observed incommensurate value for our sample of 0.356) and global phase $\phi=0$ is drawn in projection along [100] in Fig. 5b. Note that the associated composition for $\phi=0$ is $Bi_{16}Sr_{12}Fe_{28}O_{22}\square_6$ or $Bi_{4/7}Sr_{3/7}Fe_1O_{11/14}\square_{3/14}$. The reason that this is not precisely equal to the expected composition of $Bi_{0.54}Sr_{0.46}Fe_1O_{2.77}\square_{0.23}$ is that the composition of the $1\times2\times14$ commensurate approximant superstructure predicted by the superspace construction depends on the value of the global phase. Note that this is because only 14 lines or cuts through superspace are taken when it is assumed that $\gamma=\frac{5}{14}$ (these correspond to the horizontal lines shown in Fig. 6). For the actual incommensurate value of γ, i.e. $\gamma=0.356$, the whole of superspace is sampled and the composition $Bi_{0.54}Sr_{0.46}Fe_1O_{2.77}\square_{0.23}$ must necessarily be obtained. Given that the height of each Sr and oxygen vacancy domain is given by $\frac{x}{2}$ ($=0.23$ in our case) while the spacing between the superspace sampling cuts (i.e. the horizontal lines in Fig. 6) is $\frac{1}{14}$ and that $(x/2)/\frac{1}{14}=3.22$, each Sr and oxygen vacancy domain will be cut by only 3 horizontal lines 78% of the time giving rise to the *Ammm*, $1\times2\times14$, superstructure composition of $Bi_{16}Sr_{12}Fe_{28}O_{22}\square_6$ shown in Fig. 5b. The other 22% of the time, however, 4 superspace sampling cuts, or horizontal lines, will go through each Sr and oxygen vacancy domain in Fig. 6 giving rise to a second *Ammm*, $1\times2\times14$, superstructure (shown in Fig. 5c for the global phase $\phi=\frac{1}{4}$) of composition $Bi_{12}Sr_{16}Fe_{28}O_{20}\square_8$. Not surprisingly, a 78%/22% mix of these two local *Ammm*, $1\times2\times14$, superstructures corresponds to the composition $Bi_{0.54}Sr_{0.46}Fe_1O_{2.77}\square_{0.23}$. Note that the advantage of a superspace construction such as that shown in Fig. 6 is that it not only predicts the existence of both commensurate approximant superstructures, but also the order in which they occur. What then is the evidence that this predicted structure is correct?

The existence of fine scale twinning in this system (see Figs. 3 and 4; see also Fig. 2 of [10]) means that it is clearly going to be no easy task to obtain a well-refined crystal structure and, hence, to obtain the additional displacive component of the superspace AS's required for a full structural description of this solid solution phase (see e.g. [4,5]). Given this, direct evidence for the existence of the predicted pattern of Bi/Sr and oxygen vacancy ordering can

Table 2
Assumed average structure fractional co-ordinates.

Atom label	x	y	z	Occ.
$(Bi,Sr)_1$	$\frac{1}{2}$	$\frac{1}{4}$	0	$Bi_{1-x}Sr_x$
$(Bi,Sr)_2$	$\frac{1}{2}$	$\frac{3}{4}$	0	$Bi_{1-x}Sr_x$
Fe_1	0	0	$\frac{1}{2}$	1Fe
Fe_2	0	$\frac{1}{2}$	$\frac{1}{2}$	1Fe
$O1_1$	$\frac{1}{2}$	0	$\frac{1}{2}$	1O
$O1_2$	$\frac{1}{2}$	$\frac{1}{2}$	$\frac{1}{2}$	1O
$O2_1$	0	$\frac{1}{4}$	$\frac{1}{2}$	$O_{1-x/2}\square_{x/2}$
$O2_2$	0	$\frac{3}{4}$	$\frac{1}{2}$	$O_{1-x/2}\square_{x/2}$
$O3_1$	0	0	0	1O
$O3_2$	0	$\frac{1}{2}$	0	1O

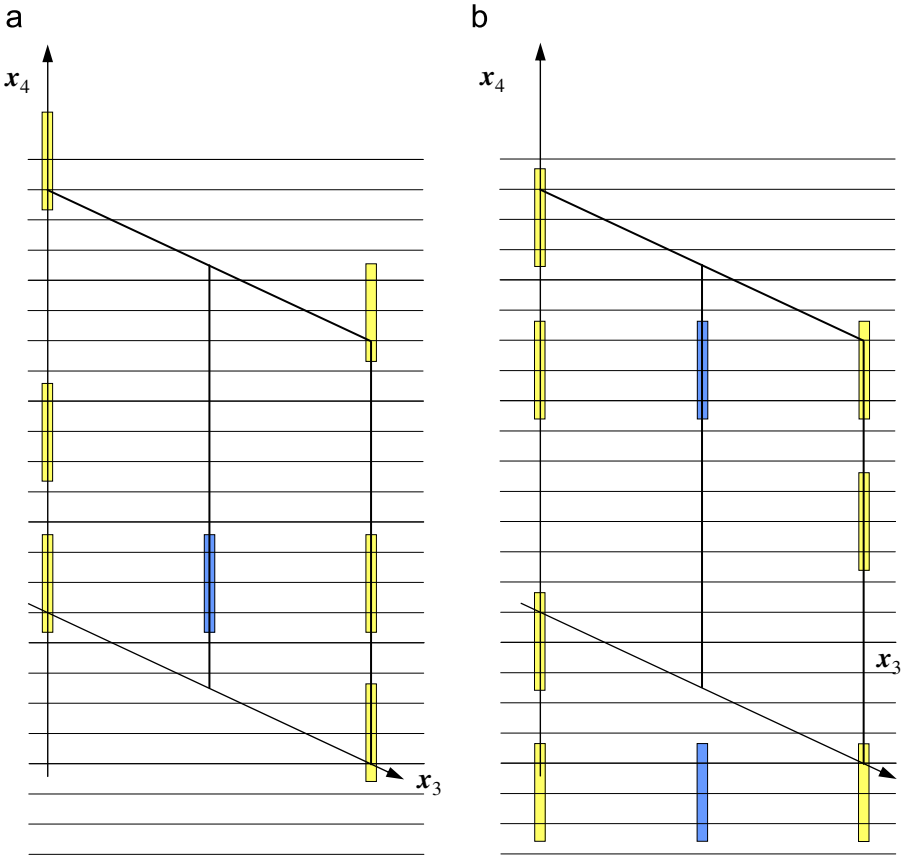

Fig. 6. (a) and (b) show the x_3–x_4 sections of the superspace atomic surfaces at $x_2=\frac{1}{4}$ (for $(Bi,Sr)_1$ and $O2_1$, with the Sr occupancy domain shown in yellow and the $O2_1$, oxygen vacancy domain shown in light blue; see Fig. 6a) and at $x_2=\frac{3}{4}$ (for $(Bi,Sr)_2$ and $O2_2$, with the Sr occupancy domain again shown in yellow and the $O2_1$, oxygen vacancy domain again shown in light blue; see Fig. 6b) drawn for $x=\frac{1}{2}$ and $\gamma=\frac{3}{8}$. (For interpretation of the references to colour in this figure legend, the reader is referred to the web version of this article.)

only really be sought from HRTEM imaging such as that shown in Fig. 3. The interpretation of such HRTEM images, however, can often be distinctly non-trivial as a result of the dependence of the image contrast upon thickness and defocus values as well as, of course, structure. Image simulations of the model structure shown in Fig. 5b are shown in projection along [100] and [010] in Figs. 7a and b, respectively, and illustrate this dependence. White dots in the simulated images were found to correspond to either columns of Bi/Sr cations (at a defocus of −11 nm), columns of Fe cations (at a defocus of −61 nm, close to the Scherzer focus of our microscope) or oxygen-deficient columns (at a defocus of −41 nm) for reasonably thin regions of crystal. The latter feature, distinctive zigzag arrays of bright white dots, is only apparent for the [100] projection and at a defocus slightly under Scherzer conditions. Figs. 7c and d show experimental HRTEM images at two defocus values for the same thin region near the edge of the specimen. The agreement between observations and simulations is reasonably good, at least on the 3–4 nm scale. In particular, the appearance of the distinct zigzag arrays of white dots just below Scherzer conditions (Fig. 7d) strongly suggests that the proposed model structure is a good approximation to the real structure.

Finally, as mentioned above, it needs to be borne in mind that the results presented in this paper are not the final story as displacive modulations accompanying the compositional ordering represented in superspace by Fig. 6 are also inevitably to be expected (see e.g. [4,5]). Unfortunately, given the current state of our structural knowledge of these materials, it is difficult to extract information about these displacements, particularly any oxygen ion displacements, from the TEM investigations in the current contribution. From the bond valence sum considerations (see Table 1) one would expect the Bi^{3+} ions to displace significantly from the centre of their cuboctahedral oxygen ion co-ordination polyhedra in an attempt to improve their inherent under-bonding giving rise to the possibility of ferroelectric behaviour. When the known magnetic behaviour of this system is also taken into account, it becomes apparent that the $(Bi_{1-x}Sr_x)Fe^{3+}_1O_{3-x/2}$, $0.2 \le x \le 0.67$, solid solution is a potential multiferroic system [22]. Further consideration, however, is beyond the scope of the current contribution.

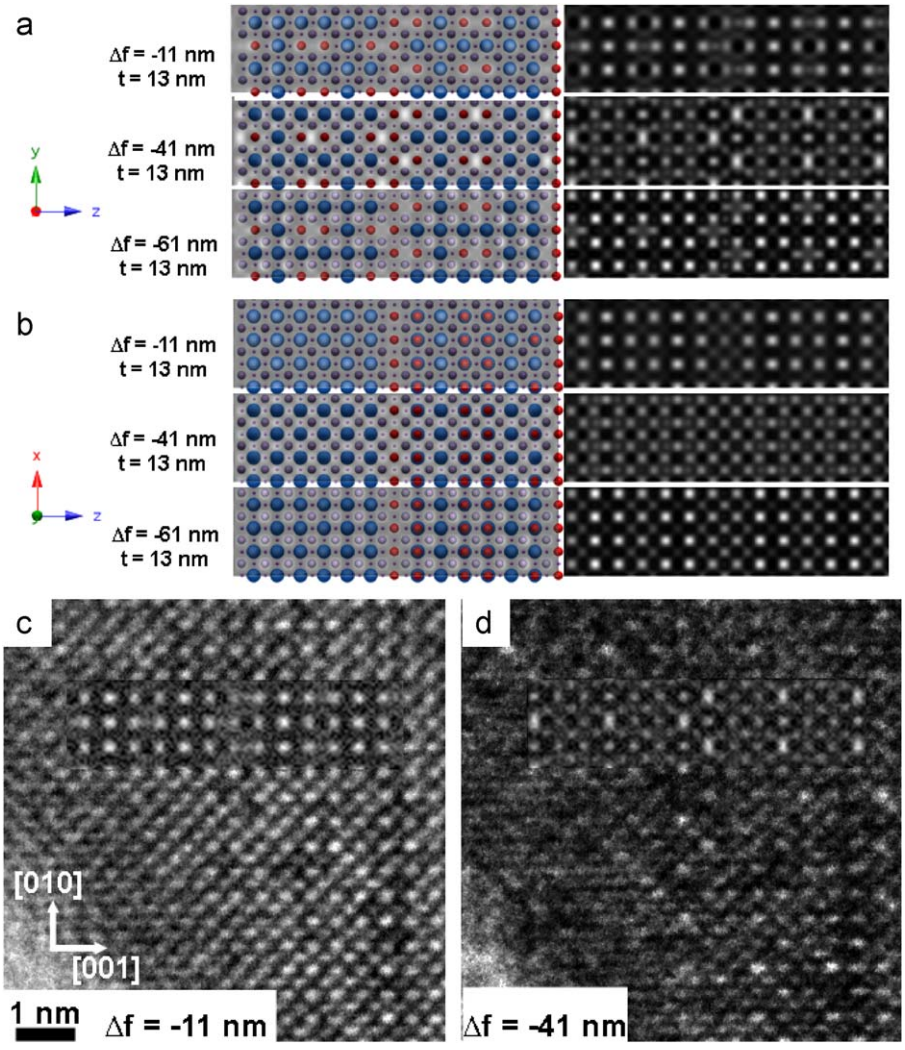

Fig. 7. (a) and (b) show HRTEM image simulations for two unit cells in projection along [100] and [010], respectively, of the model structure for different defocus values Δf and at a crystal thickness t of 13 nm. Along the [100] direction (see (a)) the oxygen-deficient columns can be imaged for certain defocus values, e.g. −41 nm (which is slightly under the Scherzer defocus of −61 nm). For other defocus values the difference between [100] and [010] views of the HRTEM images cannot be readily observed. In (c) and (d) the image simulations are compared with experimental images of the same thin region at two defocus values. The agreement is reasonably good, in particular with regards to the appearance of zigzag of white dots just under the Scherzer condition (d) These bright dots correspond to oxygen-deficient columns in the model structure.

Acknowledgments

R.L.W. acknowledges financial support from the Australian Research Council (ARC) in the form of ARC Discovery Grants. P.N.S. would like to acknowledge the Ministry of Human resource development, India for research funding.

References

[1] B. Aurivillius, Ark. Kemi 1 (1949) 463–480.
[2] R.L. Withers, J.G. Thompson, A.D. Rae, J. Solid State Chem. 94 (1991) 404–417.
[3] S.N. Ruddlesden, P. Popper, Acta Crystallogr. 11 (1958) 54–55.
[4] L. Elcoro, J.M. Perez-Mato, R.L. Withers, Z. Kristallogr. 215 (2000) 727–739.
[5] L. Elcoro, J.M. Perez-Mato, R.L. Withers, Acta Crystallogr. B 57 (2001) 471–484.
[6] J. Li, Y. Duan, H. De, D. Song, J. Alloys Compd. 315 (2001) 259–264.
[7] D. Lebeugle, D. Colson, A. Forget, M. Viret, P. Bonville, J.F. Marucco, S. Fusil, Phys. Rev. B 76 (2007) 024116.
[8] V.A. Khomchenko, D.A. Kiselev, E.K. Selezneva, J.M. Vieira, A.M.L. Lopes, Y.G. Pogorelov, J.P. Araujo, A.L. Kholkin, Mater. Lett. 62 (2008) 1927–1929.
[9] T. Zhao, A. Scholl, F. Zavaliche, K. Lee, M. Barry, A. Doran, M.P. Cruz, Y.H. Chu, C. Ederer, N.A. Spaldin, R.R. Das, D.M. Kim, S.H. Baek, C.B. Eom, R. Ramesh, Nat. Mater. 5 (2006) 823–829.
[10] C. Lepoittevin, S. Malo, N. Barrier, N. Nguyen, G. van Tendeloo, M. Hervieu, J. Solid State Chem. 181 (2008) 2601–2609.
[11] J.P. Hodges, S. Short, J.D. Jorgensen, X. Xiong, B. Dabrowski, S.M. Mini, C.W. Kimball, J. Solid State Chem. 151 (2000) 190–209.
[12] J.M. Hudspeth, D.J. Goossens, A.J. Studer, R.L. Withers, L. Norén, J. Phys. Condens. Matter 21 (2009) 124206.
[13] S.-T. Zhang, H.-W. Cheng, Y.-F. Chen, C.-H. Song, J. Wang, Y.-D. Xia, X.-N. Zhao, Z.-G. Liu, N.-B. Ming, Solid State Commun. 130 (2004) 235–239.
[14] A. Moodie, J. Cowley, Acta Crystallogr. 10 (1957) 609–619.
[15] P. Stadelmann, EMS Java Version, CIME-EPFL, CH-1015, Lausanne, Switzerland.
[16] R.L. Withers, C.D. Ling, S. Schmid, Z. Kristallogr. 214 (1999) 296–304.
[17] T. Janssen, A. Janner, A. Looijenga-Vos, P.M. de Wolff. Incommensurate and commensurate modulated structures, in: A.J.C. Wilson (Ed.), International Tables for Crystallography, vol. C, Kluwer Academic Publishers, Dordrecht, 1995, pp. 797–835.
[18] I.D. Brown, The Chemical Bond in Inorganic Chemistry. The Bond Valence Method, Oxford University Press, Oxford, 2002.
[19] M. O'Keeffe, N.E. Brese, Acta Crystallogr. B 48 (1992) 152–154.
[20] I. Etxebarria, J.M. Perez-Mato, A. Garcia, P. Blaha, K. Schwarz, J. Rodriguez-Carvajal, Phys. Rev. B 72 (2005) 174108.
[21] J.M. Perez-Mato, P. Blaha, K. Schwarz, M. Aroyo, D. Oronbegoa, I. Etxebarria, A. Garcia, Phys. Rev. B 77 (2008) 184104.
[22] K. Balamurugan, N. Harish Kumar, P.N. Santosh, J. Appl. Phys. 105 (2009) 07D909.